J Mater Sci: Mater Electron (2016) 27:10173–10179
DOI 10.1007/s10854-016-5094-0

CrossMark

Effects of sputtering power, buffer layer and film thickness on ferroelectric properties of sputtered $Bi_{0.9}Gd_{0.1}Fe_{0.9}Co_{0.1}O_3$ films

Daihong Kuang[1,2] · Ping Tang[1] · Xiaohang Wu[1] · Shenghong Yang[1] · Yueli Zhang[1]

Received: 24 December 2015 / Accepted: 30 May 2016 / Published online: 4 June 2016
© Springer Science+Business Media New York 2016

Abstract $Bi_{0.9}Gd_{0.1}Fe_{0.9}Co_{0.1}O_3$ (BGFC) films were deposited successfully on Pt(111)/Ti/SiO_2/Si(100) and $SrRuO_3$ (SRO)/Pt(111)/Ti/SiO_2/Si(100) substrates by radio frequency magnetron sputtering. Effects of sputtering power, buffer layer and film thickness on ferroelectric properties of the sputtered BGFC films were studied. X-ray diffraction demonstrated that all films had a single perovskite-type structure. Highly (012) and (024)-oriented BGFC films were formed on Pt(111)/Ti/SiO_2/Si(100) and SRO/Pt(111)/Ti/SiO_2/Si(100) substrates. The ferroelectric test indicated that the leakage current density of BGFC films sputtering at 40 W was smaller than that of BGFC films sputtering at 120 W, and its ferroelectric property was better than that of BGFC films sputtering at 120 W. Furthermore, the leakage current density of BGFC film with SRO buffer layer was improved and reduced by one order of magnitude under the same film thickness and sputtering power, comparing with the leakage current density of BGFC film without SRO buffer layer on Pt(111)/Ti/SiO_2/Si(100) substrate. The ferroelectric property of BGFC thick film is better than that of BGFC thin film under the same sputtering power and applied electric field. The log*J*–log*E* plots of BGFC films indicated that the leakage mechanisms of BGFC films with sputtering power of 40 and 120 W belong to the space-charge-limited conduction and Ohmic conduction, respectively. The mechanisms of the effects of sputtering power, buffer layer and film thickness on the ferroelectric properties of BGFC films were discussed.

✉ Yueli Zhang
stszyl@mail.sysu.edu.cn

[1] State Key Laboratory of Optoelectronic Materials and Technologies, School of Materials Science and Engineering/School of Physics, Sun Yat-Sen University, Guangzhou 510275, China

[2] School of Mathematics and Physics, Xinjiang Agricultural University, Ürümqi 830052, China

1 Introduction

Multiferroic materials, which exhibit the coexistence of ferromagnetism, ferroelectricity and/or ferroelasticity, have been studied intensively because they offer a wide range of potential applications in information storage process, spintronics, multi-state memories, as well as due to their interesting fundamental physics [1–3]. Among the multiferroics, $BiFeO_3$ (BFO) has attracted a great deal of attention after the discovery that it exhibited intrinsic large polarization (100 μC/cm^2) along [111] direction [4–6]. To date BFO is still the only known single phase multiferroic material due to its unique combination of room temperature ferroelectric (with Curie temperature $T_C \approx 810$ °C) and antiferromagnetic (with Néel temperature $T_N \approx 380$ °C) properties [1, 7].

However, the relatively modest magnetization and large leakage current observed in bulk BFO samples limit the device applications of this material. Recent studies on nanowires, nanoparticles, and thin films show the weak ferromagnetism and enhanced ferroelectric properties of BFO material owing to the size effect [8, 9]. On the other hand, the ferroelectric and magnetic properties of BFO can be modified by doping with rare-earth or alkaline earth, and transition metals either at A-site, B-site, or A–B-site [10–13]. But the effect of transition metal and rare earth ion dopants on structure and multiferroic properties of BFO thick film is rarely reported so far. Kang et al. [14] reported that the parasitic phase of γ-Fe_2O_3 had an important effect

on the magnetization of the sputtered BFO thick film, but the good ferroelectric property could not be obtained in the thick film. Lee et al. [15] reported that the resistance and capacitance of hydrothermally grown BFO thick films with compressively strained, partially relaxed epitaxial layers, and a mixture of polycrystalline and amorphous BFO layers, were significantly lower than those of the epitaxial layers, but their electric polarizations do not become saturated and show a small remnant polarization value.

Although Pradhan et al. [16–18] reported the effect of Gd doping on structural, electrical and magnetic properties of BFO electroceramics. It is observed that the materials showed room temperature enhanced electric polarization as well as ferromagnetism when rare earth ions Gd was doped in BFO. Chakrabarti et al. [19] reported that the magnetic and dielectric properties of BFO nanoparticles were enhanced by Co doping. Peng et al. [20] reported that the remanent magnetization of co-doped BFO thin film was significantly enhanced compared with that of the pure BFO film prepared under similar conditions. However, the ferroelectric property of $Bi_{0.9}Gd_{0.1}Fe_{0.9}Co_{0.1}O_3$ (BGFC) thick films fabricated by a radio frequency magnetron sputtering method has seldom been reported. Thus, the effect of Gd and Co co-doping on ferroelectric property of BFO films is ambiguous. One of our aims in the present study is that the ferroelectric property of BFO films can be further enhanced by Gd and Co co-doping at Bi–Fe-site of BFO films, in comparison with the reported data in the references [14, 15]. Another aim in this paper is that the effect of sputtering power and $SrRuO_3$ (SRO) buffer layer on ferroelectric property of BGFC films will be studied.

Thus, in this work, single-phase BGFC films have been prepared on Pt(111)/Ti/SiO_2/Si(100) and SRO/Pt(111)/Ti/SiO_2/Si(100) substrates by a radio frequency magnetron sputtering method. The effects of sputtering power, SRO buffer layer and film thicknesses on structure and ferroelectric properties of BGFC films were investigated. The results show that sputtering power, buffer layer and film thickness have an important influence on the ferroelectric properties of BGFC films.

2 Experimental procedure

All the sputtered BGFC and SRO targets used in our experiment are commercially available ones, which were synthesized by the conventional solid-state reaction method. A base pressure of 4×10^{-4} Pa was achieved before sputtering. To clean up target surface residual contaminants, a pre-sputtering of the target was carried out about 10 min prior to SRO deposition, and then SRO buffer layer ($\sim$50 nm) was sputtered on Pt(111)/Ti/SiO_2/Si(100) substrate with a substrate temperature of 650 °C using gas mixtures of Ar and O_2 (4:1) at a partial pressure of 2.2 Pa. The BGFC films were grown on Pt(111)/Ti/SiO_2/Si(100) and SRO/Pt(111)/Ti/SiO_2/Si(100) substrates by RF sputtering method with the similar sputtering conditions, respectively. The details of deposition conditions, such as substrate temperature, RF sputtering power, and deposition time, are given in Table 1. The different deposition conditions are distinguished by sample numbers (BGFC1, BGFC2, BGFC3 and BGFC4). For electrical measurements, top Pt electrodes (diameter $\sim$200 μm) were deposited on BGFC films through a mask on the films by sputtering equipment (JS-1600).

The thicknesses of BGFC films prepared on Pt(111)/Ti/SiO_2/Si(100) and SRO/Pt(111)/Ti/SiO_2/Si(100) substrates were measured by a step profiler (XP-200, AMBios). The structure of BGFC films was analyzed by an X-ray diffractometer (D-MAX 2200 VPC, RIGAKU) with Cu $K\alpha$ radiation. The polarization or leakage current density-applied field characteristics of BGFC films were obtained using a ferroelectric test system (Precision Premier II, Radiant). The surface images of BGFC films were measured by thermal FE Environment scanning electron microscope (SEM: Quanta 400, Dutch Philips).

3 Results and discussion

Figure 1 shows the X-ray diffraction (XRD) patterns of BGFC films on Pt(111)/Ti/SiO_2/Si(100) and SRO/Pt(111)/Ti/SiO_2/Si(100) substrates with sputtering power of 40 and 120 W. From XRD analysis, all BGFC samples are indexed with reference to the perovskite-type rhombohedral structure [21, 22]. Figure 1a illustrates the XRD patterns of BGFC1 and BGFC2 films grown on Pt(111)/Ti/SiO_2/Si(100) substrates with different deposition time under sputtering power of 40 W. As shown in Fig. 1a, the diffraction intensity of (012) and (024) peaks for BGFC2 film is stronger than that of BGFC1 film due to a larger thickness. Figure 1b shows the XRD patterns of BGFC3 and BGFC4 films deposited on Pt(111)/Ti/SiO_2/Si(100) and SRO/Pt(111)/Ti/SiO_2/Si(100) substrates under sputtering power of 120 W, respectively. Both films show almost the same polycrystalline structure. Highly (012) and (024) preferred orientations of BGFC4 film are more apparent than that of BGFC3 film, which indicated that SRO buffer layer was very favorable to the grain growth of BGFC film as expected. The higher crystallinity of BGFC film on SRO-buffered substrate should result from their similarity of the crystal structure and the lattice constant between SRO and BGFC.

The surface morphology of BGFC films was studied by SEM. The microscopy images are shown in Fig. 2. All films show uniform, smooth, and dense microstructure

Table 1 Deposition conditions of BGFC films by RF magnetron sputtering method

Deposition parameters	Sample nos.			
	BGFC1	BGFC2	BGFC3	BGFC4
Ceramic target	$Bi_{0.9}Gd_{0.1}Fe_{0.9}Co_{0.1}O_3$			
Deposition temperature (°C)	650	650	650	650
Base vacuum ($\times 10^{-4}$ Pa)	4	4	4	4
Working pressure (Pa)	2.2	2.2	2.2	2.2
Sputtering atmosphere (Ar:O_2)	4:1	4:1	4:1	4:1
Sputtering power (W)	40	40	120	120
Deposition time (min)	120	300	120	120
Films thickness (nm)	320	800	900	900
Bottom electrode	Pt	Pt	Pt	SRO/Pt

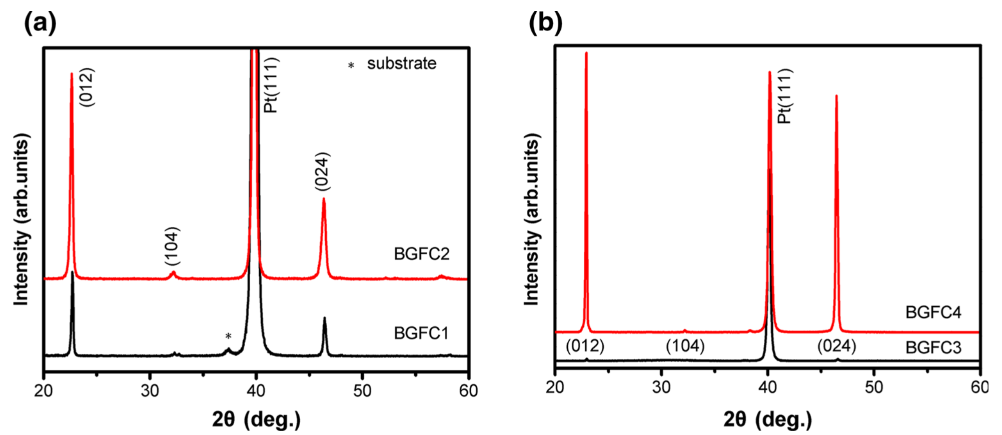

Fig. 1 XRD patterns of BGFC films with sputtering power of **a** 40 W and **b** 120 W

without porosity and crack. The statistical particle sizes of BGFC1, BGFC2, BGFC3 and BGFC4 films by using a computer software (nano measurer 1.2) are approximately 78, 97, 108, and 130 nm, respectively. The particle size scales of BGFC films indicate that sputtering power, buffer layer and film thickness have a little impact on grain structures and surface morphologies of BGFC films.

The polarization–electric field (*P*–*E*) hysteresis loops of BGFC1 and BGFC2 films measured at room temperature with different applied voltages are shown in Fig. 3a–b. Figure 3c shows the *P*–*E* hysteresis loops of BGFC2 film at 100 V with different frequencies. The inset shows that the remanent polarization of BGFC2 film decreases with the increasing of frequencies. Figure 3d shows the electric field dependence of remanent polarization in BGFC1 and BGFC2 films at 1 kHz. As evident from Fig. 3d, the remanent polarizations of BGFC1 and BGFC2 films increase monotonically with the increasing of applied electric field. However, the remanent polarization of BGFC2 film is larger than that of BGFC1 film under the same electric field due to larger grain size and thicker thickness, which is consistent with the results reported in the literatures [23–25]. The ferroelectric enhancement with thicker thickness could come from the elongation of the BGFC out-of-plane lattice constants [24] and the decreasing of the biaxial residual stress between the BGFC film and the Pt(111)/Ti/SiO_2/Si(100) substrate with increasing film thickness [25].

Figure 3e–g show the *P*–*E* hysteresis loops of BGFC3 and BGFC4 films measured at room temperature. The remnant polarizations (P_r) and coercive fields (E_c) of BGFC3 and BGFC4 at 90 V, 20 kHz are 4.87 μC/cm^2, 668 kV/cm and 7.93 μC/cm^2, 55 kV/cm, respectively. The 2P_r of BGFC4 film at 90 V, 1 kHz is 40 μC/cm^2 from Fig. 3g. Figure 3h shows the electric field dependence of remanent polarization of BGFC3 and BGFC4 films. The remanent polarizations of BGFC3 and BGFC4 films increase monotonically with the increase of applied electric field. As evident in Fig. 3h, BGFC4 film shows higher remnant polarization than that of BGFC3 film at the same electric field due to the high quality grain growth of BGFC4 film with SRO buffer layer, which is in agreement with XRD results of Fig. 1b.

Figure 4 shows the leakage current density versus applied electric field (*J*–*E*) characteristics of BGFC films. The leakage current density of each film increases monotonically at negative and positive biases as the electric field is increased. From Fig. 4a, the leakage current density of

BGFC2 film is lower than that of BGFC1 film due to thicker thickness, which can possess relatively low movable charge density near the interface [26]. The leakage current density of BGFC2 film is 7.0×10^{-7} A/cm^2 at 2.0×10^5 V/cm. At a given electric field, the leakage current density of BGFC4 film with SRO buffer layer is lower than that of BGFC3 film without buffer layer from Fig. 4b. The leakage current density of BGFC4 film is reduced by one order of magnitude compared with that of BGFC3 film. The decreased leakage current density demonstrates that SRO buffer layer plays an important role as a seed layer in stopping the charge movement from BGFC layer to bottom electrode. That is consistent with the results reported in the literature [27].

According to *J*–*E* characteristics of Fig. 4, the log*J*–log*E* plots of BGFC films are shown in Fig. 5. All logarithmic plots have been fitted by Origin software. As can be seen from Fig. 5, the log*J*–log*E* behavior shows linear characteristic with different slopes at whole electric fields. The slopes of BGFC1, BGFC2, BGFC3 and BGFC4 films are 1.80, 1.64, 1.11 and 1.13, respectively. These slope values of BGFC3 and BGFC4 films are close to one and the conduction behavior shows Ohmic conduction [28], which is dominated by thermally stimulated free electrons of BGFC3 and BGFC4 films. The injected electrons from the cathode can be swiftly transported via the conduction band, resulting in a drift current. Ohmic conduction can be expressed by $J = en\mu E$, where J is the leakage current, e is the electronic charge, n is the density of the thermally stimulated electrons, μ is the free carrier mobility, and E is the applied electric field [29]. While these values of BGFC1 and BGFC2 films are much larger than one. It means that the density of free electrons due to charge carrier injection becomes larger than the density of thermally stimulated electron in BGFC1 and BGFC2 films. Such a leakage behavior indicates a power law relationship $J \propto E^n$ (n > 1), which is a characteristic of space-charge-limited conduction (SCLC) [30, 31]. SCLC arises from a current impeding space charge forming as charges are injected into BGFC1 and BGFC2 films from the electrode at a rate faster than

Fig. 3 **a–c**, **e–g** *P*–*E* hysteresis loops of BGFC films measured in different deposition parameters and **d**, **h** the *electric field* dependence images of remanent polarization for BGFC films ▶

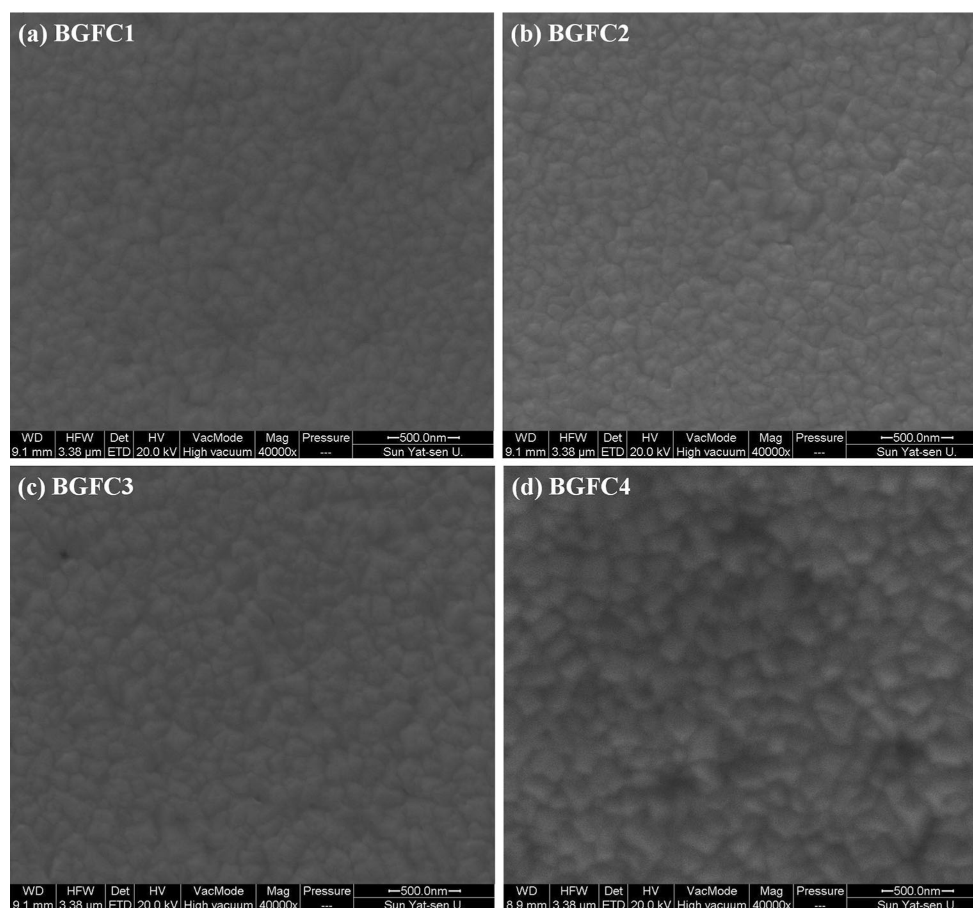

Fig. 2 Surface topographies of BGFC films

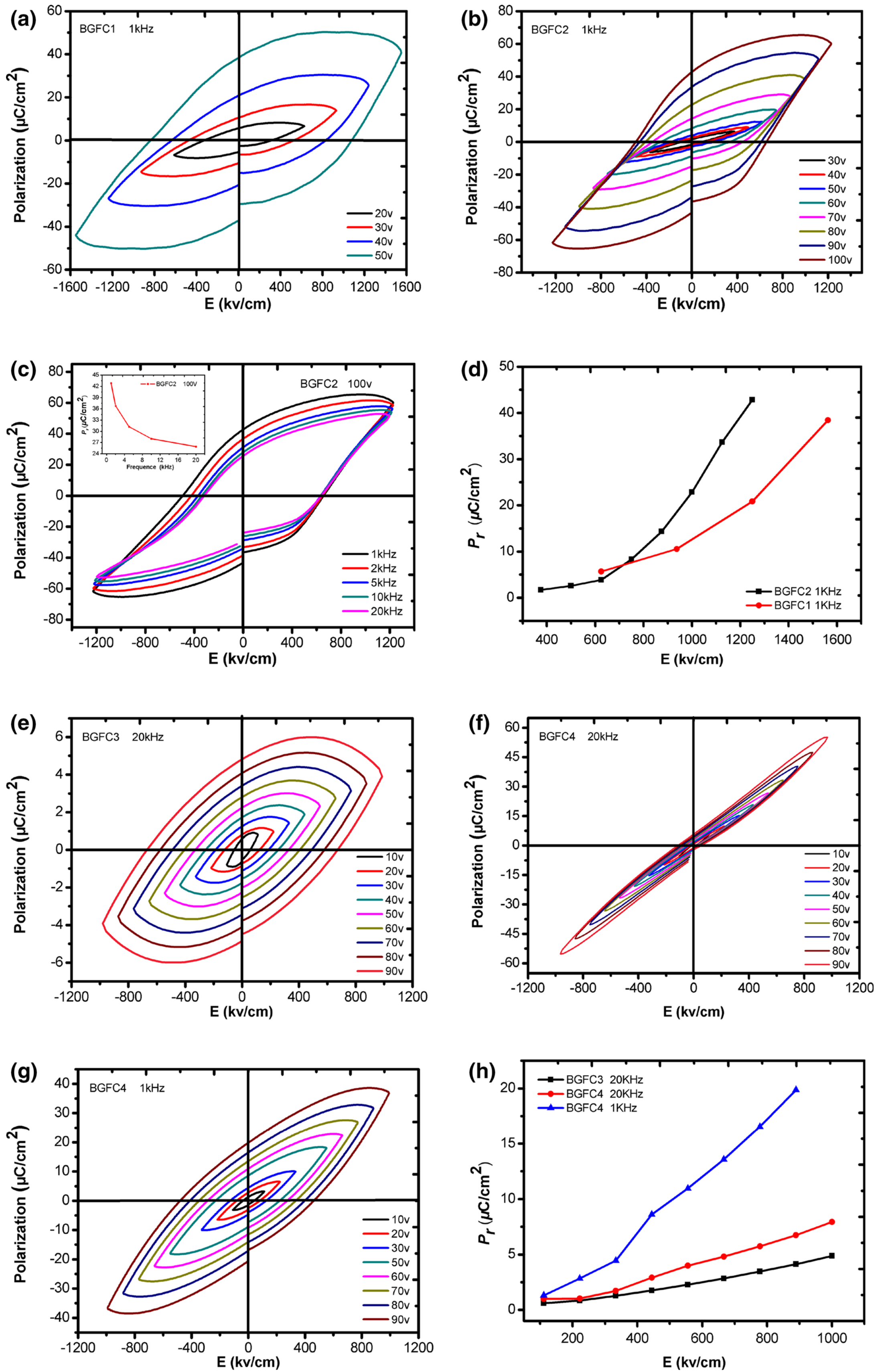

(a)
BGFC1 1kHz
Polarization (μC/cm2)
E (kv/cm)
20v
30v
40v
50v
(b)
BGFC2 1kHz
Polarization (μC/cm2)
E (kv/cm)
30v
40v
50v
60v
70v
80v
90v
100v
(c)
BGFC2 100v
BGFC2 100V
Frequence (kHz)
Polarization (μC/cm2)
E (kv/cm)
1kHz
2kHz
5kHz
10kHz
20kHz
(d)
Pr (μC/cm2)
E (kv/cm)
BGFC2 1KHz
BGFC1 1KHz
(e)
BGFC3 20kHz
Polarization (μC/cm2)
E (kv/cm)
10v
20v
30v
40v
50v
60v
70v
80v
90v
(f)
BGFC4 20kHz
Polarization (μC/cm2)
E (kv/cm)
10v
20v
30v
40v
50v
60v
70v
80v
90v
(g)
BGFC4 1kHz
Polarization (μC/cm2)
E (kv/cm)
10v
20v
30v
50v
60v
70v
80v
90v
(h)
BGFC3 20KHz
BGFC4 20KHz
BGFC4 1KHz
Pr (μC/cm2)
E (kv/cm)

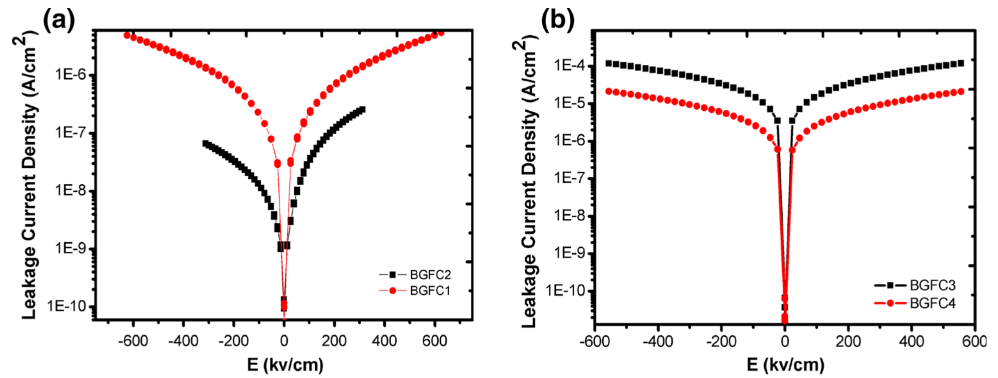

Fig. 4 The leakage current density-applied electric field behavior of BGFC films measured at room temperature

they can travel through BGFC1 and BGFC2 films [32]. The SCLC is considered as a normal leakage behavior and space charges in BFO thin films originate from traps in the band gap induced by oxygen vacancies [29, 30].

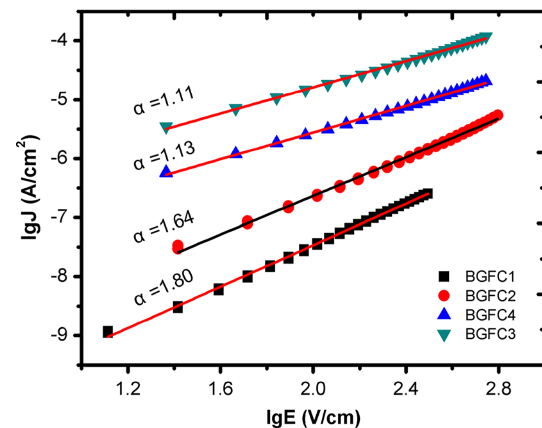

Fig. 5 The Ohmic conduction and SCLC mechanisms of BGFC films measured at room temperature

4 Conclusions

In summary, the effects of sputtering power, SRO buffer layer and thickness on the structural and ferroelectric properties of BGFC films prepared by RF magnetron sputtering method were investigated. XRD revealed that highly (012) preferred orientation BGFC films were formed on Pt(111)/Ti/SiO_2/Si(100) substrates with a perovskite-type rhombohedral structure. The preferred orientation of BGFC4 film with SRO buffer layer was more prominent. The leakage current density of BGFC films at 40w was reduced by one order of magnitude compared with that at 120w. The remnant polarization of BGFC4 film is higher than that of BGFC3 film due to the SRO buffer layer. The leakage current density of BGFC2 film was reduced by two orders of magnitude compared with that of BGFC1 film due to thicker thickness. Both low sputtering power and buffer layer can reduce the leakage current and improve the ferroelectric properties of BGFC films. The results can help guide future work to integrate the BGFC material into fundamental studies and functional microelectronic devices.

Acknowledgments This work was supported by the National Natural Science Foundation of China under Grant Nos. 61176010 and 61172027, Guangdong Natural Science Foundation under Grant No. 2014A030311049, and the Research Foundation of IARC-SYSU under Grant No. IARC 2014-09.

References

1. J. Wang, J.B. Neaton, H. Zheng, V. Nagarajan, S.B. Ogale, B. Liu, D. Viehland, V. Vaithyanathan, D.G. Schlom, U.V. Waghmare, N.A. Spaldin, K.M. Rabe, M. Wuttig, R. Ramesh, Science **299**, 1719 (2003)
2. P. Sharma, V. Verma, J. Magn. Magn. Mater. **374**, 18–21 (2015)
3. M.L. Yi, C.B. Wang, Q. Shen, L.M. Zhang, J. Mater. Sci.: Mater. Electron. **25**, 82–86 (2014)
4. P. Ravindran, R. Vidya, A. Kjekshus, H. Fjellvåg, O. Eriksson, Phys. Rev. B **74**, 224412 (2006)
5. J. Li, J. Wang, M. Wuttig, R. Ramesh, N. Wang, B. Ruette, A.P. Pyatakov, A.K. Zvezdin, D. Viehland, Appl. Phys. Lett. **84**, 5261 (2004)
6. J.B. Neaton, C. Ederer, U.V. Waghmare, N.A. Spaldin, K.M. Rabe, Phys. Rev. B **71**, 014113 (2005)
7. P. Fischer, M. Polomska, I. Sosnowska, M. Szymanski, J. Phys. C: Solid State Phys. **13**, 1931 (1980)
8. C. Ederer, N.A. Spaldin, Phys. Rev. B **71**, 060401 (2005)
9. F. Gao, Y. Yuan, K.F. Wang, X.Y. Chen, F. Chen, J.M. Liu, Z.F. Ren, Appl. Phys. Lett. **89**, 102506 (2006)
10. P. Kharel, S. Talebi, B. Ramachandran, A. Dixit, V.M. Naik, M.B. Sahana, C. Sudakar, R. Naik, M.S.R. Rao, G. Lawes, J. Phys.: Condens. Matter **21**, 036001 (2009)
11. O.D. Jayakumar, S.N. Achary, K.G. Girija, A.K. Tyagi, C. Sudakar, G. Lawes, R. Naik, J. Nisar, X. Peng, R. Ahuja, Appl. Phys. Lett. **96**, 032903 (2010)
12. Q. Zhang, C.H. Kim, Y.H. Jang, H.J. Hwang, J.H. Cho, Appl. Phys. Lett. **96**, 152901 (2010)
13. H. Deng, H.M. Deng, P.X. Yang, J.H. Chu, J. Mater. Sci.: Mater. Electron. **23**, 1215–1218 (2012)
14. L.M. Kang, W. Zhang, Y. Sun, J. Ouyang, Phys. Status Solidi A **211**, 565–569 (2014)
15. T.K. Lee, K.D. Sung, T.H. Kim, J.H. Ko, J.H. Jung, J. Appl. Phys. **116**, 194101 (2014)
16. S.K. Pradhan, B.K. Roul, J. Phys. Chem. Solids **72**, 1180–1187 (2011)

17. S.K. Pradhan, J. Das, P.P. Rout, S.K. Das, D.K. Mishra, D.R. Sahu, A.K. Pradhan, V.V. Srinivasu, B.B. Nayak, S. Verma, B.K. Roul, J. Magn. Magn. Mater. **322**, 3614–3622 (2010)
18. S.K. Pradhan, J. Das, P.P. Rout, S.K. Das, S. Samantray, D.K. Mishra, D.R. Sahu, A.K. Pradhan, K. Zhang, V.V. Srinivasu, B.K. Roul, J. Alloys Compd. **509**, 2645–2649 (2011)
19. K. Chakrabarti, B. Sarkar, V.D. Ashok, S.S. Chaudhuri, S.K. De, J. Magn. Magn. Mater. **381**, 271–277 (2015)
20. L. Peng, H.M. Deng, J.J. Tian, Q. Ren, C. Peng, Z.P. Huang, P.X. Yang, J.H. Chu, Appl. Surf. Sci. **268**, 146–150 (2013)
21. D.H. Kuang, P. Tang, S.H. Yang, Y.L. Zhang, J. Sol-Gel. Sci. Technol. **73**, 410–416 (2015)
22. P. Tang, D.H. Kuang, S.H. Yang, Y.L. Zhang, J. Alloys Compd. **622**, 194–199 (2015)
23. E.K. Akdogan, C.J. Rawn, W.D. Porter, E.A. Payzant, A. Safari et al., J. Appl. Phys. **97**, 084305 (2005)
24. Y.S. Kim, D.H. Kim, J.D. Kim et al., Appl. Phys. Lett. **86**, 102907 (2005)
25. S. Baba, J. Akedo, J. Cryst. Growth **275**, e1247–e1252 (2005)
26. M.J. Chen, J.N. Ding, J.H. Qiu, N.Y. Yuan, Mater. Lett. **139**, 325–328 (2015)
27. S. Dutta, A. Pandey, I. Yadav, O.P. Thakur, R. Laishram, R. Pal, R. Chatterjee, J. Appl. Phys. **112**, 084101 (2012)
28. H. Yang, H. Wang, G.F. Zou, M. Jain, N.A. Suvorova, D.M. Feldmann, P.C. Dowden, R.F. DePaula, J.L. MacManus-Driscoll, A.J. Taylor, Q.X. Jia, Appl. Phys. Lett. **93**, 142904 (2008)
29. C. Wang, M. Takahashi, H. Fujino, X. Zhao, E. Kume, T. Horiuchi, S. Sakai, J. Appl. Phys. **99**, 054104 (2006)
30. X.D. Qi, J. Dho, R. Tomov, M.G. Blamire, J.L. MacManus-Driscoll, Appl. Phys. Lett. **86**, 062903 (2005)
31. X. Xue, G.Q. Tan, H.F. Hao, H.J. Ren, Appl. Surf. Sci. **282**, 432–438 (2013)
32. G.W. Pabst, L.W. Martin, Y.H. Chu, R. Ramesh, J.L. MacManus-Driscoll, Appl. Phys. Lett. **90**, 072902 (2007)